Ag loaded B-doped-g C_3N_4 nanosheet with efficient properties for photocatalysis

Nirmala Thorat[a], Asha Yadav[a*], Manisha Yadav[b], Suraj Gupta[c], Ranjana Varma[d], Saju Pillai[e], Rohan Fernandes[a], Maulik Patel[c], Nainesh Patel[a,b*]

[a] *Department of Physics, University of Mumbai, Vidyanagari, Santacruz (E), Mumbai 400098, India*

[b]*National Centre for Nanosciences & Nanotechnology, University of Mumbai, Vidyanagari, Santacruz (E), Mumbai 400098, India*

[c]*School of Engineering, University of Liverpool, Liverpool, L69 3GH, UK*

[d]*Department of chemistry, Institution of chemical Technology, Matunga 400 208, India.*

[e]*Materials Science and Technology Division, CSIR-National Institute for Interdisciplinary Science and Technology, Trivandrum, Kerala, India.*

*** Corresponding author:** Asha Yadav, Nainesh Patel

E-mail: asha20yadav@gmail.com, nainesh11@gmail.com

Abstract:

Three material engineering strategies in the form of doping (Boron-doping), nanostructuring (nanosheet (NS) formation) and decorating with plasmonic nanoparticles (loading with Ag metal), were integrated to improve the photocatalytic activity of graphitic carbon nitride (gC_3N_4). Concentrations of B-doping and Ag-loading were optimized to maximize the catalytic performance in the final nanocomposite of Ag-loaded B-doped gC_3N_4 NS. Combined effect of all three strategies successfully produced over 5 times higher rate towards degradation of organic dye pollutant when compared to unmodified bulk gC_3N_4. Detailed characterization results revealed that incorporation of B in gC_3N_4 matrix reduces the band gap to increase the visible light absorption, while specific surface area is significantly enhanced upon formation of NS. Decoration of Ag nanoparticles (NPs) on B-doped gC_3N_4 NS assists in fast transfer of photogenerated electrons from gC_3N_4 to Ag NPs owing to the interfacial electric field across the junctions and thus reduces the recombination process. Investigations on individual strategies revealed that decoration of Ag NPs to induce better charge separation, is the most effective route for enhancing the photocatalytic activity.

Keywords: Graphitic carbon nitride, B doping, Ag nanoparticle, plasmonic, g-C_3N_4 nanosheet, recombination rate.

1. Introduction:

Rapid industrial growth has resulted in huge amount of waste water containing various organic and inorganic pollutants. Advanced oxidation processes (AOPs) such as photo Fenton [Pouran, et al., 2015; Pouran, et al., 2016; Pouran, et al., 2017, Pouran, et al.2018] and photocatalysis [Khaki et al., 2018; Khaki et al., 2018; Khaki et al., 2017] have proven to be highly effective methods for mineralization of these organic pollutants, among which photocatalysis has gained special interest owing to its simplicity of implementation. Photocatalysis involves three major steps 1) absorption of photons with energy greater than the band gap of the semiconductor, 2) excitation of electrons to the conduction band leaving behind holes in the valance band and 3) charge carrier transfer process, in which electrons located in conduction band are trapped by O_2 molecule adsorbed on photocatalyst to produce superoxide anion radicals. Meanwhile, holes accumulated in valence band combines with water molecule to give rise to hydroxyl radicals ($OH^{\cdot}$). These highly active radicals readily react with organic pollutant and decompose them into CO_2 and H_2O.

Several semiconductor materials such as TiO_2, ZnO, WO_3, etc. have been extensively studied for photocatalytic degradation of organic pollutants [Khaki et al., 2018; Khaki et al., 2018; Khaki et al., 2017, Sakthivel et al. 2002]. However, wide band gap and inappropriate band edge position limits their efficiency to a great extent. Recently, graphitic carbon nitride (g-C_3N_4) has gained enormous attention due to their wide application in various fields, such as decontamination of water [Gao et al., 2018; Caux et al. 2017], H_2 production via photocatalytic water splitting [Chen et al., 2018; Li et al., 2016] and electrolysis [Xu et al., 2016], etc., owing to its moderate band gap and excellent chemical stability. Nevertheless, photocatalytic efficiency of gC_3N_4 is limited due to low surface area, narrow visible light absorption and high recombination rate [Tonda et al., 2014; Hu et al., 2014]. Several strategies have been employed to overcome these limitations since its

first application for environmental issues. Stacked layered structure of gC_3N_4 leads to low surface area, thus various chemical and physical methods have been employed to break the weak Vander Waals forces between stacked layers of gC_3N_4. Exfoliation of gC_3N_4 into nanosheets (NSs) not only provides high surface area associated with large number of active sites, but is also advantageous in terms of having shorter diffusion length with low recombination rate probability compared to bulk gC_3N_4 [Niu et al., 2012]. Gao et al synthesized gC_3N_4 NS by rapid cooling treatment using liquid N_2 and demonstrated significant improvement in specific surface area (142.84 m^2/g) compared to bulk gC_3N_4 (15.67 m^2/g) and suppressed recombination rate of charge carriers. A group of researchers successfully synthesized monolayered gC_3N_4 NS using simple mixed-solvent method with superior photodegradation ability under visible light irradiation towards Rhodamine B (Rh B) [Lin et al., 2012]. The effective improvement in photoactivity was achieved owing to the favourable band structure, high surface area, prolonged lifetime of photogenerated charge carriers, high number of exposed active sites and low surface defects. Recently, easy and facile one–step approach involving acidification of melamine was proposed to prepare gC_3N_4 NSs, which revealed 3-fold increase in photocatalytic degradation rate under visible light illumination compared to gC_3N_4 [Zhang et al., 2014]. In addition to that, morphological control through post acidification, high temperature annealing and sonication in organic solvents etc. have also been reported as an efficient routes to improve the surface area of pristine gC_3N_4 [She et al., 2016; Kang et al., 2018]. Numerous efforts have been taken to synthesize different structures by modifying the surface texture of gC_3N_4 to obtain optimal photocatalyst. Chen and his group [Chen et al., 2014] reported great improvement in photodegradation ability of $gC_3N_4/Ag/TiO_2$ microspheres towards methyl orange and phenol due to efficient electron transfer process. Triple-shell gC_3N_4 nano-capsules showed superior photodegradation performance

compared to single and double-shell gC_3N_4 nano-capsule towards Rh B dye owing to improved visible light absorption and charge separation [Tong et al., 2017]. A novel hybrid architecture of mesoporous gC_3N_4 with $BiPO_4$ nanorods displayed significant improvement in photocatalytic degradation of methyl orange dye due to ultrafast migration of charge carriers at the interface [Li et al., 2014].

The strategy of doping with metals [Deng et al., 2016; Sun et al, 2015] and non-metals [Zhu et al., 2015; Sagra et al., 2016] has also proven to be an excellent method for band gap engineering in order to extend light absorption ability in visible region. It was observed that anion doping induces conduction band tuning through hybridization between p orbital of doped element and C atom present in gC_3N_4 matrix. On the other hand, cation doping modifies valance band edge by forming discrete band of 3d orbitals of transition element. It was found that boron doping lowers valence band position of resulting material and hence increases the potential oxidation strength of photogenerated holes as compared to gC_3N_4 [Sagara et al., 2016]. Yan et al. described that boron doping promotes photodegradation of pollutants by improving the dye adsorption and light absorption ability. Superior photocatalytic removal of $UO_2^{2+}$was reported for B-doped gC_3N_4 due to band gap narrowing [Lu et al., 2016]. High concentration of boron doping leads to formation of ternary compound boron carbon nitride (BCN), possessing properties of boron nitride and gC_3N_4 [Sivaprakash et al., 2018]. Depending upon the concentration of B, C and N, properties such as electron affinity, bandgap (0-5.5 eV) and effective barrier potential varies [Sivaprakash et al., 2018]. Hu et al. demonstrated significant improvement in photocatalytic performance of Fe doped bulk gC_3N_4 compared to gC_3N_4 for both degradation of organic pollutant and water splitting process, however low surface area of Fe doped gC_3N_4 limits its photocatalytic performance. It has been established that addition of Fe and P codopant in gC_3N_4 photocatalyst results in enhanced

surface area, extended visible light absorption and narrowing of band gap in addition to decreased electron-hole pair recombination rate, thus exhibiting much higher Rh B photodegradation rate [Hu et al., 2014].

The issue of high recombination rate in gC_3N_4 can be suppressed by noble metal loading on gC_3N_4 surface, or coupling it with other semiconductors such as TiO_2, graphene oxide, carbon nanodots etc [Li et al., 2017; Xiang et al., 2011; Dadigala et al., 2017]. Bu et.al. [Bu et al., 2014] prepared Ag modified gC_3N_4 which displayed significant improvement in electron hole pair separation with prolonged lifetime. Ge and his [Ge et al., 2011] group synthesized Ag loaded gC_3N_4 and reported substantial enhancement in photocatalytic performance which was attributed to enhanced visible light absorption and efficient migration of photogenerated charge carriers. Ag loaded gC_3N_4 was also prepared by Zhang et al. [Zhang et al., 2016] by photo-deposition method under ambient condition which showed improved photodegradation performance than pure gC_3N_4 as a result of close contact between Ag and gC_3N_4 and localized surface plasmon resonance (SPR) of Ag. Cheng et al. [Chang et al., 2013] found that Pd decorated gC_3N_4 facilitates efficient separation of photoelectrons and holes through electron trapping on Pd^0 atom.

There are very few reports that involves combining two of the above mentioned three strategies to modify gC_3N_4 and improve its photocatalytic performance. Li et al. [Li et al., 2017] synthesized Ti^{3+}-TiO_2 decorated exfoliated oxygen doped gC_3N_4 and showed remarkable increase in photocatalytic activity due to combined effect of efficient photogenerated electron hole pair separation and decreased charge carrier resistance at the interface. B-doped gC_3N_4 in form of nanosheets showed 12 times better photocatalytic performance for H_2 evolution as compared to pristine gC_3N_4 [Thaweesak et al., 2017], due to the synergistic effect of enhanced visible light absorption and higher surface area. Dadigala et al. [Dadigala et al., 2017] synthesized gC_3N_4 NS

and decorated it with carbon dots as well as Ag nanoparticles to provide improved separation of photogenerated carriers and enhanced visible light absorption.

To the best of our knowledge, there is scarcity of report combining all the above-mentioned strategies to improve the photocatalytic properties of gC_3N_4. The present work aims not only to extend visible light absorption but also to enhance electron-hole pair separation and achieve higher active surface area. Therefore in this work, boron doped gC_3N_4 was first synthesized to narrow the band gap. Subsequently, Ag NPs were decorated over B doped gC_3N_4 to reduce electron hole pair recombination rate. In order to achieve higher active surface area with more number of exposed active sites, bulk gC_3N_4 was exfoliated to obtain nanosheet form. Thus, the present report gives a comprehensive study of combining all the above-mentioned strategies and its effect to improve the performance of gC_3N_4 towards degradation of industrial dyes. This form of gC_3N_4 showed over 5 times superior photodegradation performance compared to bulk gC_3N_4 towards Rh B under light illumination. Role of each of the strategies in enhancing photocatalytic activity of Ag NPs loaded B-doped gC_3N_4 NS compared to bulk gC_3N_4 is explained using various characterization techniques.

2. Experimental methods:

2.1 Materials

Melamine (pure) ($C_3H_6N_6$, ≥ 99%) was purchased from Loba chemie laboratory reagents and fine chemicals. Boric acid (H_3BO_3, 99.5%) and Silver nitrate (extrapure) ($AgNO_3$, 99.8%) were purchased from S.D. Fine-Chem Limited. Rh B (AR) was obtained from central drug house private limited. Nitric acid (HNO_3, 65 wt%) was obtained from Merck life science private limited. Ethanol (99.9 %) was purchased from Changshu Hongsheng fine chemicals. All the above mentioned

reagents used in the present work were of analytically pure grade and were used without any further purification.

2.2 Synthesis of photocatalyst materials:

2.2.1 Bulk g-C_3N_4 & B-doped-gC_3N_4:

B-doped-gC_3N_4 was synthesized by thermal polymerization of melamine at high temperature in a programmable furnace. In brief, required amount of boric acid (H_3BO_3) was dissolved in 50 ml of ethanol followed by addition of 4gm of melamine powder and dispersed through ultrasonic treatment. The quantity of H_3BO_3 was selected to obtain 4, 6, 8 and 10 at.% of Boron in final gC_3N_4 powder. The mixture was stirred for 15 minutes at room temperature and then dried at 80^{o}C. This dried mixture was transferred to a ceramic crucible with cover lid and calcinated in air at 650^{o}C for 4h with a ramp rate of 3°C/min. After calcination, a yellowish orange compound of B-doped-gC_3N_4 was obtained, which was grounded into fine powder. Pure gC_3N_4 powder was also prepared by using the same procedure without the addition of boron precursor.

2.2.2 gC_3N_4 & B-doped-gC_3N_4 NS:

gC_3N_4 and B-doped-gC_3N_4 NS were prepared by liquid exfoliation of the as-prepared powders in diluted HNO_3. In detail, 500 mg of as synthesized powder was dispersed in 30 ml HNO_3 (65 wt%) and stirred for 7h at room temperature to weaken the bonds between interlayers. This solution was diluted, using 200 ml double distilled water (DDW) and ultrasonicated for 16 hours to exfoliate the gC_3N_4 layers. The suspension was separated from residual solution and washed with DDW and ethanol several times to remove any residual acid. Finally, the mixture was dried at 80 ^{o}C to obtain NSs of gC_3N_4 & B-doped-gC_3N_4. The obtained powder was light yellowish orange in colour.

2.2.3 Ag loaded B-gC_3N_4:

100 mg of B-doped-gC_3N_4 (bulk or nanosheet) and appropriate amount (5, 10 & 15 mg) of silver nitrate ($AgNO_3$) was dispersed in 25 ml of ethanol and stirred for 5 h at room temperature. Finally, the suspension was dried at 80 ^oC to obtain Ag metal loaded B-gC_3N_4.

2.3 Characterization of samples:

To identify the different phases and crystalline structure in the samples, X-ray diffraction (XRD) measurements were performed on a XRD-6100 (Shimadzu) instrument with a Cu K_α source (Applied voltage & current values of 30 kV & 30 mA). The morphology of the samples were investigated by JEOL (2100F Cs corrected) Field emission gun based transmission electron microscope (FEG-TEM) using an accelerating voltage of 200 kV. Brunauer-Emmett-Teller (BET) specific surface area of the catalyst was measured by nitrogen (N_2) adsorption-desorption isotherms at -196 ^oC on a BET surface area system (Smart SORB 93) after degassing all samples at 150 ^oC for 3h. The optical absorption spectra of the samples were measured using a Cary 500 UV-vis-NIR spectrometer in diffuse reflectance mode in the range of 200-800 nm. Photoluminescence (PL) studies were carried out using fluorescence spectrophotometer (Varian, Cary Eclipse). The emission spectra was collected at an excitation wavelength of 385nm. The average lifetime of charge carriers of the samples was examined by Time resolved photoluminescence (TRPL) spectroscopy (ISS chronos BH model). To acquire PL and TRPL spectra, 2 mg powder catalyst was dispersed in 10ml of DDW and transferred into a 1cm x 1cm cuvette for measurement. The chemical state and surface composition of the samples was studied by X-ray photoelectron spectroscopy (XPS) (PHI 5000 Versaprobe scanning ESCA microprobe) equipped with a monochromatic Al K_α (1486.6 eV) X-ray source and a hemispherical analyzer.

Appropriate electrical charge compensation was employed to perform the analysis and binding energy was referenced to the C 1s peak.

2.4 Photocatalytic performance:

The photocatalytic performance of all the samples were carried out in a vertical photoreactor set up using 150W Xenon lamp (Hamamatsu) as a source of light. Typically, to study photocatalytic activity, 10 mg of photocatalyst sample was dispersed in 50 ml aqueous suspension solution of Rh B (10 mg/ L) via ultrasonic treatment for 5 mins. Prior to photocatalytic degradation test, the suspension was kept under constant stirring for 30 mins in dark in order to achieve adsorption-desorption equilibrium between photocatalyst and dye. During light irradiation, after each successive time interval, 2 ml of suspension was drawn and centrifuged to separate supernatant from photocatalyst powder. The concentration of dye in residual solution was evaluated by recording intensity of the absorption band of Rh B at 547 nm using UV-Vis spectrophotometer (Implen). Throughout the experiment, the pH of the solution was maintained to neutral and activity was performed in ambient condition. For the complete duration of the experiment, the distance between surface of suspension solution and source of light was kept constant and equal to 47cm. In order to discard the possibility of self-degradation of dye under light illumination, blank test of Rh B suspension solution was performed in the absence of photocatalyst powder. All the tests were repeated at least twice to confirm the obtained results.

3. Results and Discussion:

Three material engineering strategies were integrated in order to solve the most basic problems of gC_3N_4 photocatalyst i.e. high recombination rate of photogenerated charges, absorption of a narrow region of the visible light and low surface area with limited number of

active sites. Firstly, boron was doped in gC_3N_4 which is expected to replace C in the matrix; secondly, this B-doped-gC_3N_4 is exfoliated to form NSs and lastly decorate this doped-NS with plasmonic materials in the form of Ag NPs. However, before combining all three strategies, each step is optimized before moving to the next. It is also important to investigate the effect of each strategies in the nanocomposite, thus the combinations of two strategies were also studied before preparing the final composite.

gC_3N_4 was first mono doped with four different concentrations of boron (4, 6, 8 & 10 at.%) in order to select the optimum concentration for preparing nanocomposite. The range of doping was chosen such that boron is doped in the matrix of gC_3N_4 rather than forming segregated boron species over gC_3N_4 sheets. The optimization of B concentration was done on the basis of the photocatalytic performance for degradation of Rh B dye. By measuring the relative intensity of the peak at ~547nm with respect to time, the decrease in Rh B dye concentration was estimated. Self-degradation of Rh B dye was found to be negligible under the light irradiation in the absence of photocatalyst. Among the different concentrations, boron doping of 8 at.% shows the best photocatalytic activity (Fig. S1) with 1.8 times higher rate of degradation than undoped gC_3N_4. This optimized B-doped gC_3N_4 was later converted into 'single layer' or 'few layers based NS' using acid treatment followed by exfoliation under ultrasonication for long duration of time (16 hr). Different amount of Ag metal NPs (3, 6 or 9 wt.%) were loaded over B-doped gC_3N_4 NS and it was discovered that for each loading amount, the photocatalytic activity increases as compared to B-doped gC_3N_4 NS and undoped gC_3N_4 NS (Fig. S2). However, no major variation was observed within all three loading concentrations and thus a minimum loading of 5 wt.% was selected as the optimized loading. Further studies were carried out on samples namely, bulk g-C_3N_4, B-doped gC_3N_4 bulk, undoped gC_3N_4 NS, B-doped gC_3N_4 NS, Ag NPs loaded over B-gC_3N_4

bulk and Ag NPs loaded over B-gC_3N_4 NS which are henceforth recognized as bulk gC_3N_4, B-bulk-gC_3N_4, NS-gC_3N_4, B-NS-gC_3N_4, Ag-B-bulk-gC_3N_4 and Ag-B-NS-gC_3N_4 respectively.

Structural modification of gC_3N_4 was studied by XRD and reported in Fig.1. Two characteristic peaks with a strong intensity at 27.6^o and a weak signal at 12.9^o corresponding to (002) and (100) planes of gC_3N_4 (JCPDS-87-1526) were observed for all six samples. The peak at 27.6° corresponds to a characteristic interlayer stacking reflection and the one at 12.9° represents the in plane structural packing motif of the heptazine units. As compared to bulk-gC_3N_4, the peak intensity of the main (002) peak is reduced in case of NS-gC_3N_4, suggesting a decrease in the number of layers in the stacking. In all B-doped gC_3N_4 samples, the same peak is slightly shifted to higher angle by 0.2^o, thus indicating that B is incorporated in the gC_3N_4 lattice causing a structural variation.

The optical properties were investigated by using UV-vis spectroscopy in diffuse reflectance mode (Fig. 2) and the corresponding band gap was estimated using Tauc plot. The band gap of bulk-gC_3N_4 was determined to be about 2.77eV which is in close proximity to other reports on gC_3N_4 [Zou et al., 2018] and its theoretically reported value of 2.7eV [Kaining et al., 2016]. Upon B-doping, the band edge shifts marginally towards the longer wavelength with a weak tail in the visible region. This feature again confirms the presence of B in gC_3N_4 lattice where B, by replacing C, forms localized electronic states within the band gap [Kaininf et al., 2016] and contributes in enhancing the visible light absorption. The band edge is slightly blue shifted upon formation of NS (NS-gC_3N_4 and B-NS-gC_3N_4), which is expected due to the quantum confinement effect in nanostructures. When Ag NPs are decorated over NS and bulk B-doped-gC_3N_4, the band edge is red shifted mainly by the contribution of the surface plasmonic band of Ag NPs in the

range of 420-520 nm. This shows that both B and Ag are beneficial for gC_3N_4 in absorbing visible light which further assists in photocatalytic reaction.

XPS spectra of C1s, N1s, Ag 3d and B1s levels for all the six samples are displayed in Fig.3. Bulk-gC_3N_4 showed typical three peaks in C1s band at 284.6 eV, 288.2 eV, and 286.2 eV attributed to adventitious carbon bond (C-C), carbon bonded to nitrogen in sp^2 bonds (C-N-C) and trace amount of C-O bond respectively. As samples were calcinated in air, small amount of C-O is formed on the surface of the catalysts. Same set of peaks are present for all other samples irrespective of the type of strategies used to modify gC_3N_4. In case of N 1s level, four peaks due to, C-N=C at 398.7 eV, N-$(C)_3$ at 399.7 eV, C-H-N at 401.1eV, and N-O at 404.2eV are present in all samples. The XPS peak of surface boron is distinctly visible only for the gC_3N_4 samples in the form of NS (B-NS-gC_3N_4 and Ag-B-NS-gC_3N_4) (Fig. 3). For B-doped bulk-gC_3N_4, the signal is very weak and cannot be distinguished evidently from the background. Single peak at 192.0 eV is detected in B 1s spectrum of B-NS-gC_3N_4 and Ag-B-NS-gC_3N_4 samples, which is attributed to C-NB group for B-doped-gC_3N_4. The spectrum of Ag 3d band (Fig. 3) is composed of two peaks at 368.5 and 374.5 eV with a spin energy separation of 6.0 eV. Both these peaks are standardized binding energy (BE) of Ag $3d_{5/2}$ and Ag $3d_{3/2}$ levels of metallic silver. The XPS results indicate that the chemical structure of gC_3N_4 remains intact upon doping with B and Ag loading. Boron is incorporated in the gC_3N_4 matrix by replacing C and forms B-N bonds which are exposed on the surface only upon the formation of NS. On the contrary, metallic Ag NPs are decorated over the gC_3N_4 bulk as well as on NS.

TEM images of bulk-gC_3N_4, NS-gC_3N_4, B-NS-gC_3N_4 and Ag-B-NS-gC_3N_4 are shown in Fig. 4. Morphology of B-bulk-gC_3N_4 and Ag-B-bulk-gC_3N_4 was similar to bulk-gC_3N_4, thus was not shown here. Sheet-like morphology is clearly visible for bulk-gC_3N_4 (Fig. 4a), with length of

a few microns (1-2 µm), thus showcasing the graphitic nature. Upon formation of NS (Fig. 4b), the length reduces in the range of 100-400 nm which is further reduced to below 100 nm for NS of B-doped-gC_3N_4 (Fig. 4c). No major variation in the average length of NS is observed upon Ag loading (Fig. 4d). On comparing the HRTEM images of B-NS-gC_3N_4 (Fig. 4e) and Ag-B-Ns-gC_3N_4 (Fig. 4f), dark spot of diameter 5-10 nm is observed in latter, due to the presence of Ag NPs decorated on gC_3N_4 NS. For these NPs, an interplanar spacing of 0.24 nm was measured from the lattice fringes, which is attributed to (111) planes of metallic Ag. Morphological analysis by TEM clearly confirms the formation of NS which is decorated with Ag NPs in Ag-B-NS-gC_3N_4.

To verify the effect of nanosheet formation on the overall surface area of gC_3N_4, BET surface area was measured and summarised in Table1. In comparison to bulk samples (bulk-gC_3N_4, B-bulk-gC_3N_4 and Ag-B-bulk-gC_3N_4), the surface area is drastically improved for same samples in the form of NS (NS-gC_3N_4, B-NS-gC_3N_4 and Ag-B-NS-gC_3N_4). The highest surface area is recorded for B-NS-gC_3N_4 (57.3 m^2/g), which decreases by a small amount (49.6 m^2/g) upon loading with Ag NPs for Ag-B-NS-gC_3N_4 sample. It was also noticed that addition of B and Ag in bulk-gC_3N_4 disrupts the interlayer to increase the surface area by a small amount for Ag-B-bulk-gC_3N_4.

The effect of B and Ag on recombination of photogenerated charges can be qualitatively studied by measuring the emission radiation generated by the recombination process. PL spectra of all six samples were recorded at an excitation wavelength of 385 nm and is shown in Fig. 5. The intensity of the peak centred at 465 nm, due to band edge emission, is lower for NS-gC_3N_4 when compared to its bulk counterpart. This is mainly due to the shorter path length required for the photogenerated charges in case of NS. Upon boron doping, the intensity further reduces, thus indicating that boron doped in gC_3N_4 lattice can act as the trapping site for charges, resulting in

reduced recombination process. However, lowest intensity of the PL peak is detected after loading with Ag NPs in both the cases of bulk and NS of B-doped-gC_3N_4. Thus, Ag in form of plasmonic NPs are highly effective in decreasing the recombination of photogenerated electron and hole pairs, owing to the electronic levels of Ag and gC_3N_4. Fermi level of Ag lies in between conduction band (CB) and valence band (VB) of gC_3N_4, which leads to migration of electrons from gC_3N_4 to Ag when junction between Ag and gC_3N_4 is formed. This electron transfer leads to band bending at the CB which generates electric field across junction. During light irradiation, the photogenerated electrons are unidirectionally transferred from CB of gC_3N_4 to Ag NPs under the influence of interfacial electric field resulting in better charge separation. To investigate the lifetime of charge carriers, time resolved photoluminescence (TRPL) spectra were acquired for all the samples. The decay curve was fitted using three components to obtain average lifetime of charge carriers. The average lifetime of bulk gC_3N_4 (1.45 ns) is increased to 2.05 ns when all three strategies are integrated in Ag-B-NS-gC_3N_4 sample, thus suggesting that both Ag and B effectively delay the recombination processes, with Ag being more efficient than B.

The photocatalytic activity of all the samples for degradation of Rh B dye was tested and presented in Fig. 6. Except for bulk gC_3N_4, all other modified samples were able to complete the degradation within the maximum time limit of 180 min, thus showing improved activity than bulk. Duration of 180, 160, 120, 80 and 60 mins were required by B-bulk-gC_3N_4, NS-gC_3N_4, B-NS-gC_3N_4, Ag-B-bulk-gC_3N_4 and Ag-B-NS-gC_3N_4 to complete the reaction. The highest photocatalytic performance was obtained when all the three strategies of B-doping, NS formation and Ag loading were combined in Ag-B-NS-gC_3N_4 photocatalyst to produce 5.2 times higher reaction rate than bulk-gC_3N_4. When single strategy was adopted to modify gC_3N_4, for the case of B-doped-gC_3N_4 and NS-gC_3N_4, the activity is improved by 1.8 and 2 times, respectively, as

compared to bulk gC_3N_4. This result indicates that NS formation is more efficient in improving the photocatalytic activity than B-doping. When two strategies were combined in the form of B-NS-gC_3N_4 and Ag-B-bulk-gC3N4 samples, the reaction rate increases by 2.6 and 4.2 times, respectively. This indicates that loading Ag is even more effective strategy in enhancing the photocatalytic activity.

Photocatalytic reactions are mainly driven by three factors - surface area, charge separation and visible light absorption capability of photocatalyst material. Thus, adopting a single strategy can improve only one of these factors, such as B-doped-gC_3N_4 and NS-gC_3N_4 increases the visible light absorption and surface area (as confirmed by UV-vis-spectroscopy and BET surface area), respectively. When both of these strategies are combined together in B-NS-gC_3N_4, surface area as well as visible light absorption increases, thus leading to higher activity as compared to individual strategy. As explained earlier, Ag NPs are very efficient in improving the charge separation by creating interfacial electric field across the junction with gC_3N_4 to cause fast transfer of photogenerated electrons from CB of gC_3N_4 to Ag NPs, avoiding recombination process. At the same time, plasmonic Ag NPs are also capable of creating intense SPR-induced electromagnetic field to increase the rate of electron-hole formation on the surface of gC_3N_4 in vicinity of Ag NPs. This mechanism assists in further improvement of the photocatalytic activity. Therefore, when Ag is loaded on B-NS-gC_3N_4, all three strategies create a synergic effect to promote the necessary features resulting in remarkable photocatalytic activity. The effect of Ag is also noticeable when loaded on B-bulk-gC_3N_4 in Ag-B-bulk-gC_3N_4 showing second best activity among all combinations. The important point to be noticed from above results is that Ag loading turns out to be the most effective strategy in increasing the activity and hence charge recombination seems to be the rate limiting process for photocatalytic reaction.

The mechanism involved in Ag-B-NS-gC_3N_4 for degradation of pollutant is schematically presented in Fig 7. Briefly, upon light irradiation Ag-B-NS-gC_3N_4, creates electron and hole pairs in gC_3N_4. The photogenerated electrons are immediately transferred from CB of gC_3N_4 to Ag NPs due to the electric field created at their interface, whereas photogenerated holes are left in the VB of gC_3N_4. The electrons on the Ag NPs react with adsorbed oxygen on the surface to form superoxide radicals ($O_2^{\bullet -}$), while holes on gC_3N_4 readily react with surface bonded OH^- to form hydroxyl radical species ($OH^{\bullet}$). Both these species are highly oxidizing species and are very active for the degradation process. In this mechanism, the present form of photocatalyst is very useful mainly considering the role of each engineering strategies involved. The B-doping is able to improve visible light absorption as confirmed by UV-vis spectra, thus producing large number of electron and hole pairs. It is also observed in PL spectra that B-doping decreases the recombination process by small amount. High surface area in case of nanosheet provides large number of active sites to promote photocatalytic reaction. On the other hand, Ag seems to be very proficient in separating electron and hole pair by generated electric field across the metal-semiconductor junction. Due to SPR effect, Ag NPs absorbs visible light to create extra electrons to produce higher number of superoxide radicals. The electromagnetic field generated by SPR effect of plasmonic Ag NPs is also able to create more electron-hole pairs across gC_3N_4 surface. All these stimulating effects generated in Ag-B-NS-gC_3N_4 assist the photo-degradation reactions in an outstanding manner.

4. Conclusion:

In summary, combination of three strategies has been employed to synthesize efficient Ag-B-NS-gC_3N_4 photocatalyst with enhanced visible light absorption, surface area, and electron hole pair separation. Thorough characterization studies show that B-doping results in superior photocatalytic performance with better visible light absorption capability. Subsequent acid treatment of B-gC_3N_4 to synthesize nanosheets resulted in higher exposed specific surface area with large number of active sites for organic pollutant adsorption during photocatalysis reaction. On the other hand, successive Ag loading has proven to be a highly effective strategy to facilitate efficient charge carrier transport and prolong charge carrier lifetime as a consequence of better electron-hole pair separation at the interface of gC_3N_4 and Ag NPs due to the interfacial electric field. On comparison of photocatalytic activity, it was found that B-gC_3N_4, B-NS-gC_3N_4 and Ag-B-NS-gC_3N_4 show 1.8, 2.6 and 5.2 times higher photocatalytic performance compared to pure gC_3N_4, respectively. This implies that combined effect of all the three strategies has great influence on enhancing the degradation ability of resultant photocatalyst with highest contribution from loading of Ag NPs.

Acknowledgements:

Asha Yadav and Nainesh Patel acknowledge WOS-A scheme (SR/WOS-A/PM-116/2016) under DST for their financial support. Ranjana Varma thanks WOS-A scheme (SR/WOS-A/PM-5/2017) for providing financial assistance. Nainesh Patel acknowledge UGC and SERB-DST for providing financial support through Faculty recharge program and Extra Mural project (FILE NO. EMR/2016/003028). Suraj Gupta acknowledges the research grant from UK Commonwealth Commission through Commonwealth Rutherford Fellowship (INRF-2017-139). Maulik Patel acknowledges the seed funding obtained from EPSRC-GCRF No. 141131/155337.

References

1. Bu, Y., Chen, Z., Li, W., 2014. Using electrochemical methods to study the promotion mechanism of the photoelectric conversion performance of Ag-modified mesoporous g-C_3N_4heterojunction material. Appl. Catal. B:Envion. 144, 622-630.
2. Caux, M., Fina, F., Irvine, J., Idriss, H., Howe, R., 2017. Impact of the annealing temperature on Pt/g-C_3N_4 structure, activity and selectivity between photo-degradation and water splitting. Catalysis Today 287, 182-188.
3. Chang, C., Fu, Y., Hu, M., Wang, C., Shan, G., Zhu, L., 2013. Photodegradation of bisphenol A by highly stable palladium-doped mesoporous graphite carbon nitride (Pd/mpg-C_3N_4) under simulated solar light irradiation. Appl. Catal B: Environ, 142–143, 553-560.
4. Chen, P., Xing, P., Chen, Z., Lin, H., He, Y., 2018. Rapid and energy-efficient preparation of boron doped g-C_3N_4 with excellent performance in photocatalytic H_2-evolution. Intern. J. Hydrogen Energy 43, 19984-19989.
5. Dadigala, R., Bandi, R., Gangapuram, B.,Guttena, V.,2017. Carbon dots and Ag nanoparticles decorated g-C_3N_4 nanosheets for enhanced organic pollutants degradation under sunlight irradiation. J. Photo Chem. Photobio A: Chem342, 42-52.
6. Deng, L., Zhu, M., 2016. Metal–nitrogen (Co-g-C_3N_4) doping of surface-modified single-walled carbon nanohorns for use as an oxygen reduction electrocatalyst. RSC Adv. 6, 25670-25677.
7. Donga, F., Lia, Y., Wanga, Z., Ho, W., 2015. Enhanced visible light photocatalytic activity and oxidation ability of porous graphene-like g-C_3N_4nanosheets via thermal exfoliation. Appl. Surf. Sci. 358, 393-403.

8. Gao, M., Feng, J., Zhang, Z., Gu, M., Wang, J., Zeng, W., Lv, Y., Ren, Y., Wei, T., Fan, Z., 2018. Wrinkled Ultrathin Graphitic C_3N_4 Nanosheets for Photocatalytic Degradation of Organic Waste Water. ACS Appl. Nano. Mater. 1, 6733-6741.
9. Ge, L., Han, C., Liu, J., Li, Y., 2011. Enhanced visible light photocatalytic activity of novel polymeric g-C_3N_4 loaded with Ag nanoparticles. Appl. Catal A: Gener.409-410, 215-222.
10. Hu, S., Jin, R., Lu, G., Liu, D., Gui, J., 2014. The properties and photocatalytic performance comparison of Fe^{3+}-doped g-C_3N_4 and Fe_2O_3/g-C_3N_4 composite catalysts. RSC Adv. 4, 24863-24869.
11. Hu, S., Ma, L., You, J., Li, F., Fan, Z., Lu, G., Liu, D., Gui, J., 2014. Enhanced visible light photocatalytic performance ofg-C_3N_4 photocatalysts co-doped with iron and phosphorus. Appl. Surf. Sci. 311, 164-171.
12. Jiang, L., Yuan, X., Pan, Y., Liang, J., Zeng, G., Wu, Z., Wang, H. 2017. Doping of graphitic carbon nitride for photocatalysis: A review. Appl. Catal B: Environ, 217, 388-406.
13. Kaining, D., Wen, L., Huang, M., Zhang, Y., Lu, Y., Chen, Z., 2016. How does the B, F-monodoping and B/F-codoping affect the photocatalytic water-splitting performance of g-C_3N_4. Phys. Chem. Chem. Phys.18, 19217-19226.
14. Kang, S., Zhang, L., He, M., Zheng, Y., Cui, L., Sun, D., Hu, Bing., 2018. Alternated cooling and heating" strategy enables rapid fabrication of highly-crystalline g-C_3N_4 nanosheets for efficient photocatalytic water purification under visible light irradiation. Carbon 137, 19-30.

15. Khaki M.R.D., Shafeeyan M.S., Raman A.A.A., Daud W.M.W.A, 2018. Evaluating the efficiency of nano-sized Cu doped TiO_2/ZnO photocatalyst under visible light irradiation. J Mol Liq. 258, 354–365.

16. Khaki M.R.D., Shafeeyan M.S., Raman A.A.A, Daud W.M.W.A., 2018. Enhanced UV–Visible photocatalytic activity of Cu-doped ZnO/TiO_2 nanoparticles, J Mater Sci: Mater Electron. 29, 5480–5495.

17. Khaki M.R.D., Shafeeyan M.S., Raman A.A.A., Daud W.M.W.A., 2017. Application of doped photocatalysts for organic pollutant degradation- A review, J Environ Manag. 198, 78-94.

18. Le, S., Jiang, T., Zhao, Q., Liu, X., Li, Y., Fang,B., Gong, M., 2016. Cu-doped mesoporous graphitic carbon nitride for enhanced visible-light driven photocatalysis. RSC Adv. 6, 38811–38819.

19. Li, K., Huang, Z., Zeng, X., Huang, B., Gao, S., Lu, J., 2017. Synergetic Effect of Ti^{3+} and Oxygen Doping on Enhancing Photoelectrochemical and Photocatalytic Properties of TiO_2/g-C_3N_4 Heterojunctions. ACS Appl. Mater & Interfaces, 9, 11577-11586.

20. Li, Y., Wu, S., Huang, L., Wang, J., Xu, H., Li, H.,2014. Synthesis ofcarbon-dopedg-C3N4 composites with enhanced visible-light photocatalytic activity. Mater. Lett.137, 281–284.

21. Li, Z., Chao, C., Lu, G., 2016. Visible Photocatalytic Water Splitting and Photocatalytic Two-Electron Oxygen Formation over Cu- and Fe-Doped g-C_3N_4. J. Phys. Chem. C120, 56–63.

22. Li, Z., Kong, C., Lu, G., 2016. Visible Photocatalytic Water Splitting and Photocatalytic Two-Electron Oxygen Formation over Cu and Fe Doped C_3N_4. J. Phys. Chem. C 120, 56-63.

23. Lin, Q., Li, L., Liang, S., Liu, M., Bi, J., Wu, L., 2015. Efficient synthesis of monolayer carbon nitride 2D nanosheet with tunable concentration and enhanced visible-light photocatalytic activities. Appl. Catal. B: Environ. 163, 135–142.

24. Liu, Q., Chen, T., Guo, Y., Zhang, Z., Fang, X., 2017. Grafting Fe(III) species on Carbon Nanodots/Fe-doped g-C_3N_4 via Interfacial Charge Transfer Effect for Highly Improved Photocatalytic Performance. Appl. Catal. B: Environ.205, 173-181.

25. Lu, C., Chen, R., Wu, X., Fan, M., Liu, Y., Le, Z, Jiang, S., Song, S., 2016. Boron doped g-C_3N_4 with enhanced photocatalytic UO_2^{2+} reduction performance. Appl. Surf. Sci. 360, 1016–1022.

26. Niu, P., Zhang, L., Liu, G., Cheng, H., 2012. Graphene-Like Carbon Nitride Nanosheets for Improved Photocatalytic Activities. Adv. Funct. Mater. 22, 4763-4770.

27. Pouran, S.R., Aziz, A.R.A., Daud, W.M.W.A., Shafeeyan, M.S., 2015. Effect of niobium and molybdenum impregnation on adsorption capacity and Fenton catalytic activity of magnetite. RSC Adv. 106, 87535-87549.

28. Pouran S.R., Bayrami A., Aziz A.R.A., Daud W.M.W.A, Shafeeyan M.S., 2016. Ultrasound and UV assisted Fenton treatment of recalcitrant wastewaters using transition metal-substituted-magnetite nanoparticles. J Mol Liq. 222, 1076–1084.

29. Pouran S.R., Bayrami A., Raman A.A.a, Daud W.M.W.A., Shafeeyan M.S., Khataee A., 2018. Comprehensive study on the influence of molybdenum substitution on characteristics and catalytic performance of magnetite nanoparticles, Res. Chem. Inter, 44, 883–900.

30. Pouran S.R., Bayrami A., Shafeeyan M.S., Raman A.A.A., Daud W.M.W.A., 2018. A Comparative study on a cationic dye removal through homogeneous and heterogeneous Fenton oxidation systems. Acta Chim. Slov. 65, 166–171.

31. Sakthivel S., U. Geissen S., Bahnemann D., Vogelpohl V., 2002. Enhancement of photocatalytic activity by semiconductor heterojunctions: α-Fe_2O_3, WO_3 and CdS deposited on ZnO, J Photochem Photobio A: Chem. 148, 283-293.

32. Shivprakash, K., Induja, M., Priya, P., 2018. Facile synthesis of metal free non-toxic Boron Carbon Nitride nanosheets with strong photocatalytic behavior for degradation of industrial dyes. Materials research Bulletin. 100, 313-321.

33. Seredych, M., Bandosz T J., 2016. Nitrogen enrichment of S-doped nanoporous carbon by g-C_3N4: Insight into photosensitivity enhancement. Carbon 107, 895-906.

34. Thaweesak, S., Wang, S., Lyu, M., Xiao, M., Peerakiatkhajohn, P., Wang, L., 2017. Boron-doped graphitic carbon nitride nanosheets for enhanced visible light photocatalytic water splitting. RSC Dalton Trans.46, 10714-10720.

35. Tonda, S., Kumar, S., Kandula, S., Shanker, V., 2014. Fe-doped and -mediated graphitic carbon nitride nanosheets for enhanced photocatalytic performance under natural sunlight. J. Mater. Chem. A2, 6772-6780.

36. Tong, Z., Yang, D., Li, Z., Nan, Y., Ding, F., Shen, Y., Jiang, Z., 2017. Thylakoid-Inspired Multishell g‑C_3N_4Nanocapsules with Enhanced Visible-Light Harvesting and Electron Transfer Propertiesfor High-Efficiency Photocatalysis. ACS Nano.11, 1103−1112.

37. Sagara, N., Kamimura, S., Tsubota, T., Ohno, T., 2016. Photoelectrochemical CO_2 reduction by a p-type boron-doped g-C_3N_4 electrode under visible light. Appl. Catal B: Environ, 192, 193-198.

38. She, X., Liu, L., Ji, H., Mo, Z., Li, Y., 2016. Template-free synthesis of 2D porous ultrathin nonmetal-doped g-C_3N_4nanosheets with highly efficient photocatalytic H_2 evolution from water under visible light. Appl. Catal. B: Environ.187, 144-153.

39. She, X., Xu, H., Xu, Y., Yan, J., Xia, J., Xu, L., Song, Y., Jiang, Y., Zhang, Q., Li, H., 2014. Exfoliated Graphene-Like Carbon Nitride in organic solvents: the enhanced photocatalytic activity and highly selective and sensitive sensor for the detection of trace amount of Cu^{2+}. J. Mater. Chem. A2, 2563-2570.

40. Sun, J., Fu, Y., He, G., Sun, X., Wang, X., 2015. Green Suzuki–Miyaura coupling reaction catalyzed by palladiumnano particles supported on graphitic carbon nitride. Appl. Catal. B Environ. 165, 661–667.

41. Wang, J., Cui, C., Li, Y., Liu, L., Zhang, Y., Shi, W., 2017. Porous Mn doped g-C_3N_4 Photocatalysts for enhanced synergetic degradation under visible-light illumination. J. Hazardous Mater. 339, 43-53.

42. Xiang, Q., Yu, J., Jaroniec, M., 2011. Preparation and enhanced visible-light photocatalytic H_2-production activity of graphene/C_3N_4 Composites. J. Phys. Chem. C115, 7355–7363.

43. Xu, Y., Kraft, M., Xu, R., 2016. Metal-free carbonaceous electrocatalysts and photocatalysts for water splitting. Chem. Soc. Rev. 45, 3039-3052.

44. Yan, S., Li, Z., Zou, Z., 2010. Photodegradation of rhodamine B and methyl orange over Boron-dopedg-C_3N_4 under visible light irradiation. Langmuir 26, 3894–3901.x

45. Zhang, X., Hu, J., Jiang, H., 2014. Facile modification of a graphitic carbon nitride catalyst to improveits photo reactivity under visible light irradiation. Chem. Eng. J.256, 230–237.

46. Zhao, S., Zhang, Y., Zhou, Y., Wang, Y., Qiu, K., Zhang, C., Fang J., Sheng, X., 2018. Facile one-step synthesis of hollow mesoporous g-C_3N_4 spheres with ultrathin nanosheets for photoredox water splitting. Carbon 126, 247-256.

47. Zhou, Y., Zhang,L., Huang,W., Kong,Q., Fan,X., Wang, M., Shi, J., 2016. N-doped graphitic carbon-incorporated g-C_3N_4 for remarkably enhanced photocatalytic H_2 evolution under visible light. Carbon 99, 111-117.

48. Zhu, Y-P.,Ren, T-Z., Yuan, Z-Y., 2015. Mesoporous Phosphorus-Doped g‑C_3N_4 Nanostructured Flowers with Superior Photocatalytic Hydrogen Evolution Performance. ACS Appl. Mater. Interfaces 7, 16850−16856.

49. Zhu, Y-P., Ren, T-Z., Yuan, Z-Y., 2015. Mesoporous Phosphorus-Doped g‑C_3N_4 Nanostructured Flowers with Superior Photocatalytic Hydrogen Evolution Performance. ACS Appl. Mater. Interfaces 7, 16850−16856.

50. Zou, J., Wu, S., Liu, Y., Sun, Y., Cao, Y., Hsu J-P, Wee A. T. S., Jiang, J., 2018. An ultra-sensitive electrochemical sensor based on 2D g-C_3N_4/CuO nanocomposites for dopamine detection. Carbon 130, 652-663.

Figure caption:

Figure 1: XRD pattern of bulk-gC_3N_4, NS-gC_3N_4, B-bulk-gC_3N_4, B-NS-gC_3N_4, Ag-B-bulk-gC_3N_4 and Ag-B-NS-gC_3N_4 samples.

Figure 2: UV-vis absorption spectra in diffuse reflectance mode of bulk-gC_3N_4, NS-gC_3N_4, B-bulk-gC_3N_4, B-NS-gC_3N_4, Ag-B-bulk-gC_3N_4 and Ag-B-NS-gC_3N_4 samples.

Figure 3:XPS spectra of C1s and N1s of (a)bulk-gC_3N_4, (b) NS-gC_3N_4, (c) B-bulk-gC_3N_4, (d) B-NS-gC_3N_4, (e) Ag-B-NS-gC_3N_4 and (f) Ag-B-bulk-gC_3N_4 samples, Ag 3d of (a) Ag-B-NS-gC_3N_4 and (b) Ag-B-bulk-gC_3N_4 and B 1s of (a) Ag-B-NS-gC_3N_4 and (b) B-NS-gC_3N_4.

Figure 4: TEM images of (a) bulk-gC_3N_4, (b) NS-gC_3N_4, (c) B-NS-gC_3N_4 and (d) Ag-B-NS-gC_3N_4 and HRTEM images of (e) B-NS-gC_3N_4 and (f) Ag-B-NS-gC_3N_4.

Figure 5: Photoluminescence emission spectra of bulk-gC_3N_4, NS-gC_3N_4, B-bulk-gC_3N_4, B-NS-gC_3N_4, Ag-B-bulk-gC_3N_4 and Ag-B-NS-gC_3N_4 samples.

Figure 6: Comparison of photocatalytic degradation of Rh B under light irradiation in presence of bulk-gC_3N_4, NS-gC_3N_4, B-bulk-gC_3N_4, B-NS-gC_3N_4, Ag-B-bulk-gC_3N_4 and Ag-B-NS-gC_3N_4 samples.

Figure 7: Mechanism involving charge separation in Ag loaded B-NS-gC_3N_4 during photodegradation of Rh B under light illumination.

Table 1: BET surface area and average lifetime of bulk-gC_3N_4, NS-gC_3N_4, B-bulk-gC_3N_4, B-NS-gC_3N_4, Ag-B-bulk-gC_3N_4 and Ag-B-NS-gC_3N_4 samples.

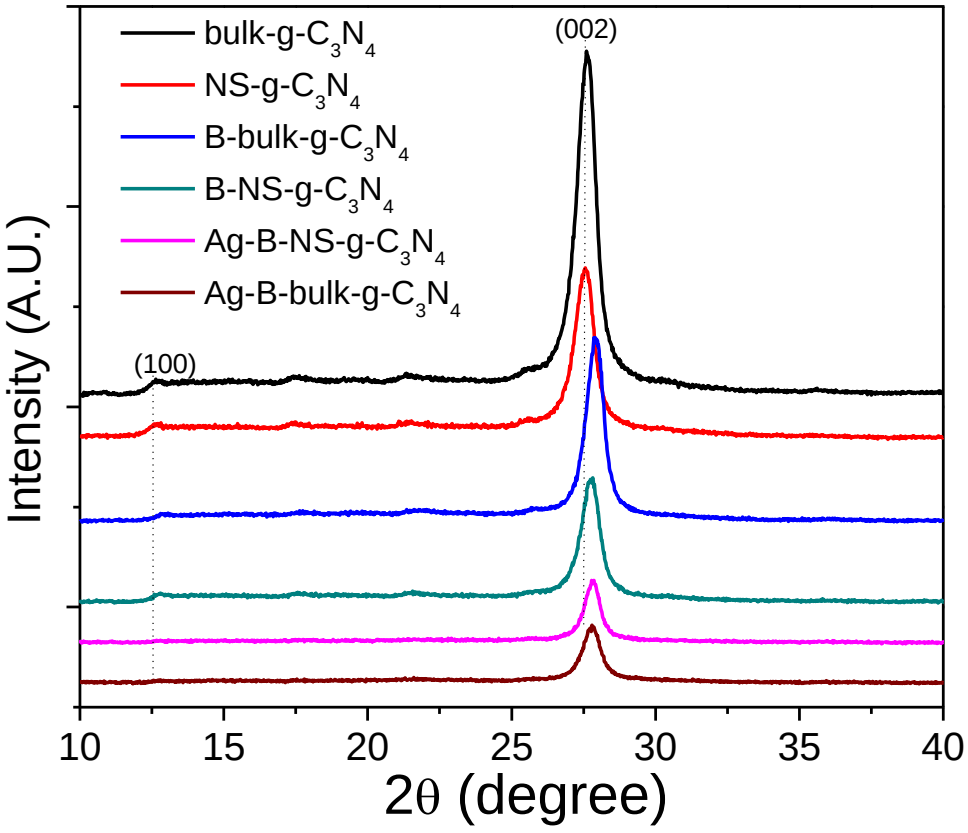

Fig. 1: XRD pattern of bulk-gC_3N_4, NS-gC_3N_4, B-bulk-gC_3N_4, B-NS-gC_3N_4, Ag-B-bulk-gC_3N_4 and Ag-B-NS-gC_3N_4 samples.

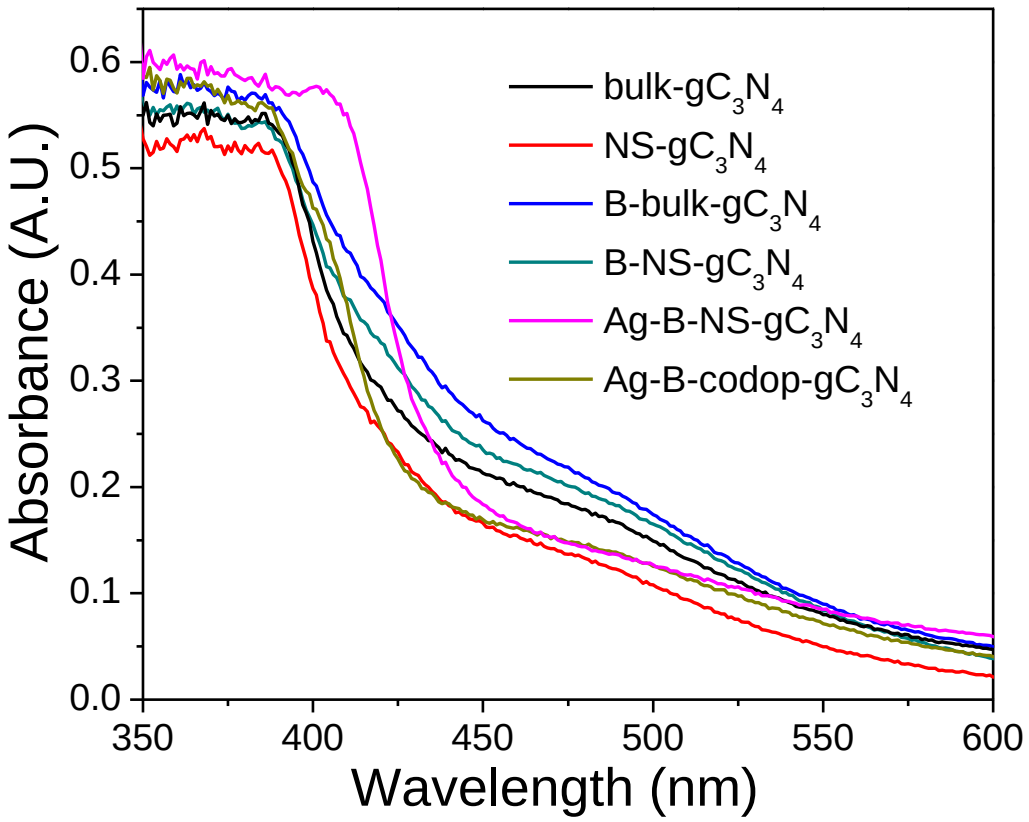

Fig. 2: UV-vis absorption spectra in diffuse reflectance mode of bulk-gC_3N_4, NS-gC_3N_4, B-bulk-gC_3N_4, B-NS-gC_3N_4, Ag-B-bulk-gC_3N_4 and Ag-B-NS-gC_3N_4 samples.

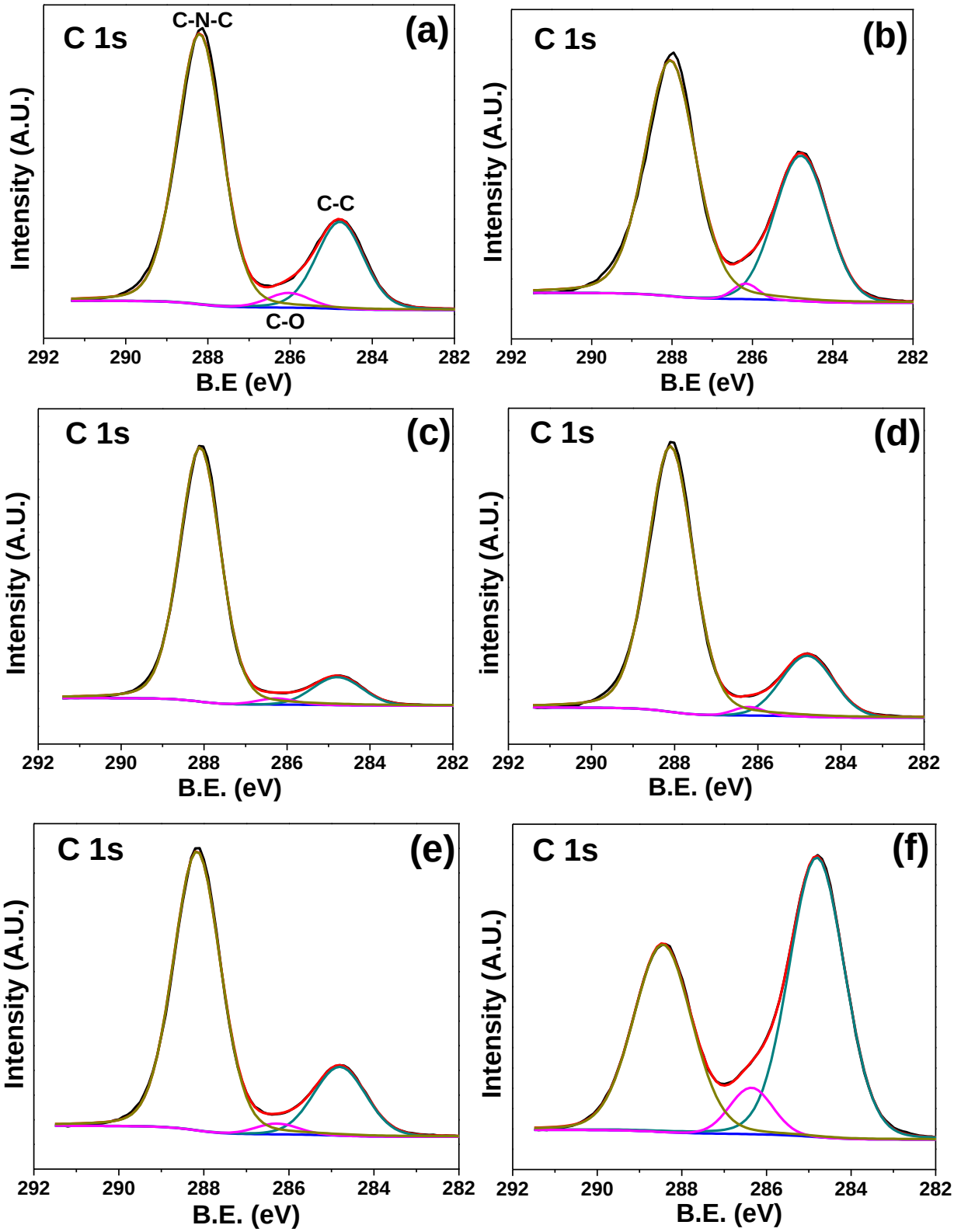
C 1s
(a)
C-N-C
C-C
C-O
Intensity (A.U.)
292
290
288
286
284
282
B.E (eV)
C 1s
(b)
Intensity (A.U.)
B.E (eV)
C 1s
(c)
Intensity (A.U.)
B.E. (eV)
C 1s
(d)
intensity (A.U.)
B.E. (eV)
C 1s
(e)
Intensity (A.U.)
B.E. (eV)
C 1s
(f)
Intensity (A.U.)
B.E. (eV)

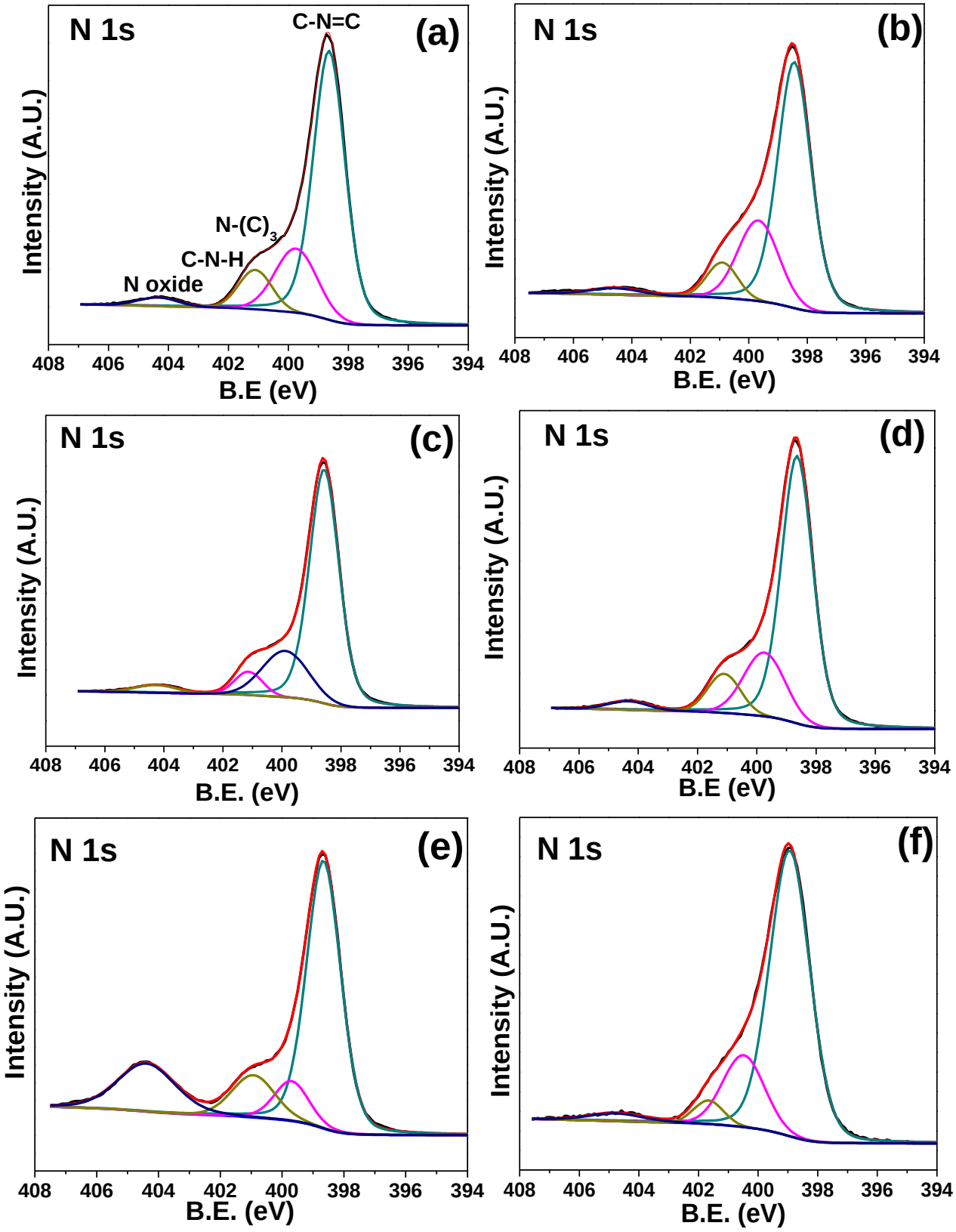
N 1s
(a)
C-N=C
N-(C)3
C-N-H
N oxide
Intensity (A.U.)
B.E (eV)
(b)
B.E. (eV)
(c)
(d)
(e)
(f)
408
406
404
402
400
398
396
394

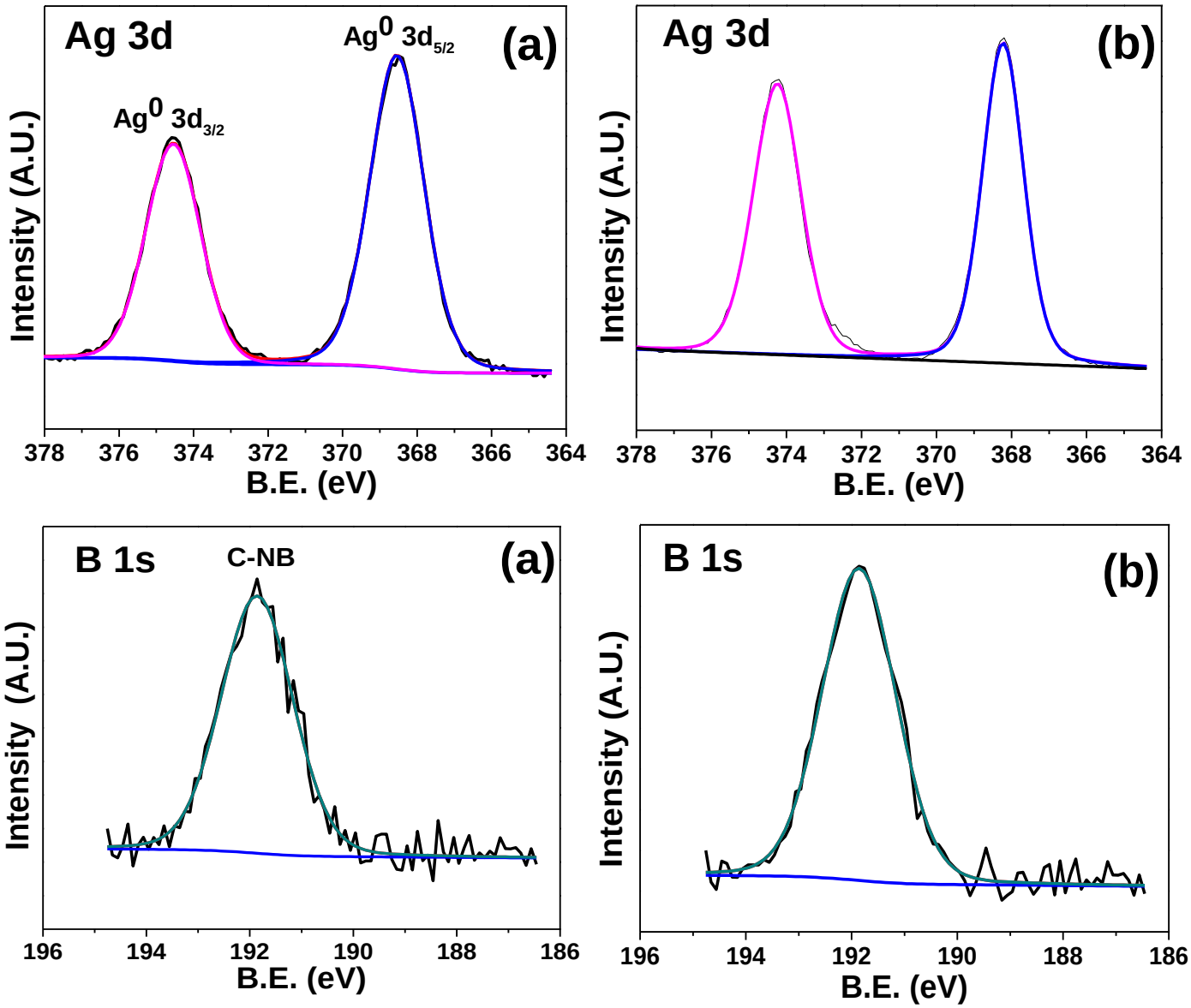

Fig. 3: XPS spectra of C1s and N1s of (a) bulk-gC_3N_4, (b) NS-gC_3N_4, (c) B-bulk-gC_3N_4, (d) B-NS-gC_3N_4, (e) Ag-B-NS-gC_3N_4 and (f) Ag-B-bulk-gC_3N_4 samples, Ag 3d of (a) Ag-B-NS-gC_3N_4 and (b) Ag-B-bulk-gC_3N_4 and B 1s of (a) Ag-B-NS-gC_3N_4 and (b) B-NS-gC_3N_4.

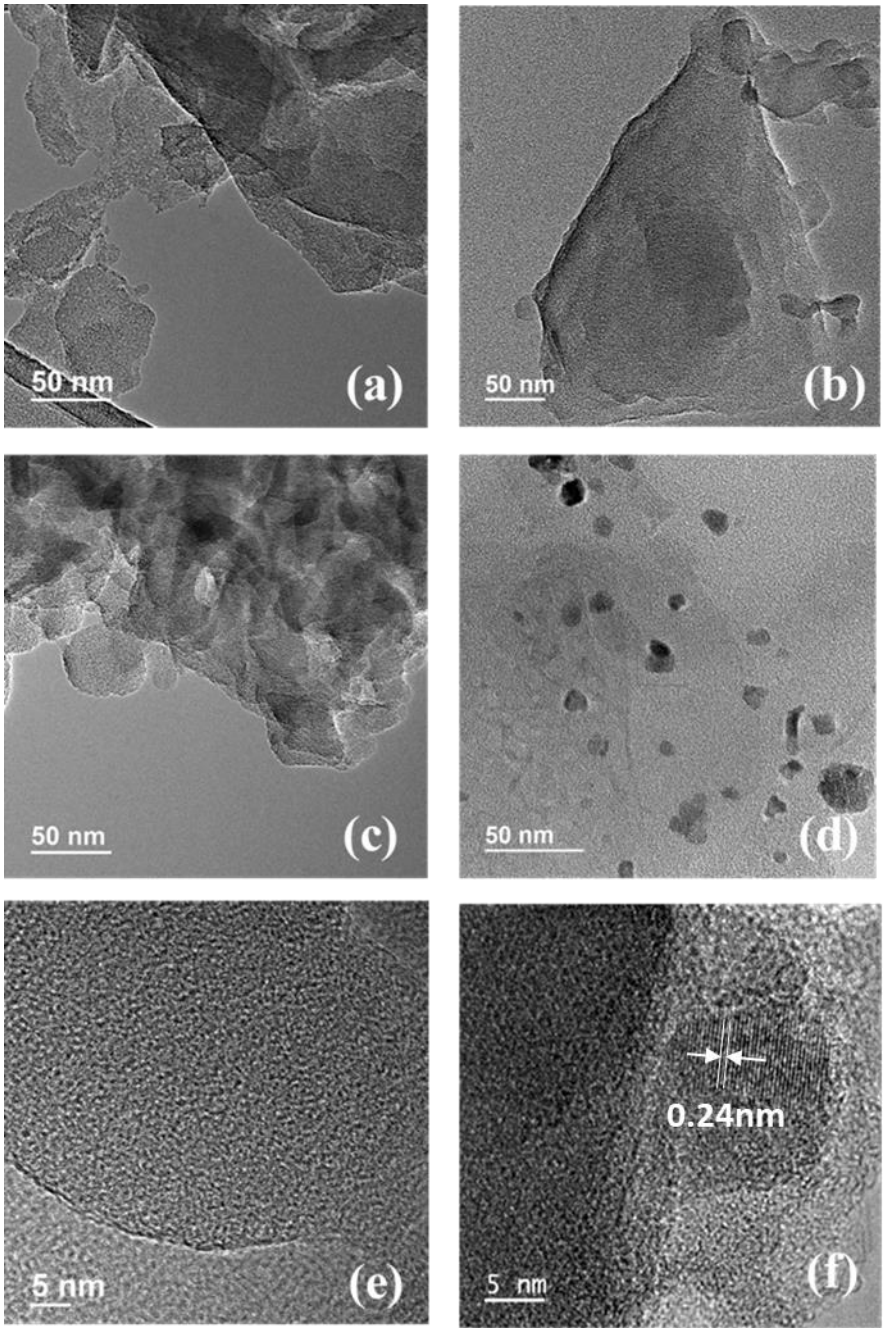

Fig. 4: TEM images of (a) bulk-gC_3N_4, (b) NS-gC_3N_4, (c) B-NS-gC_3N_4 and (d) Ag-B-NS-gC_3N_4 and HRTEM images of (e) B-NS-gC_3N_4 and (f) Ag-B-NS-gC_3N_4.

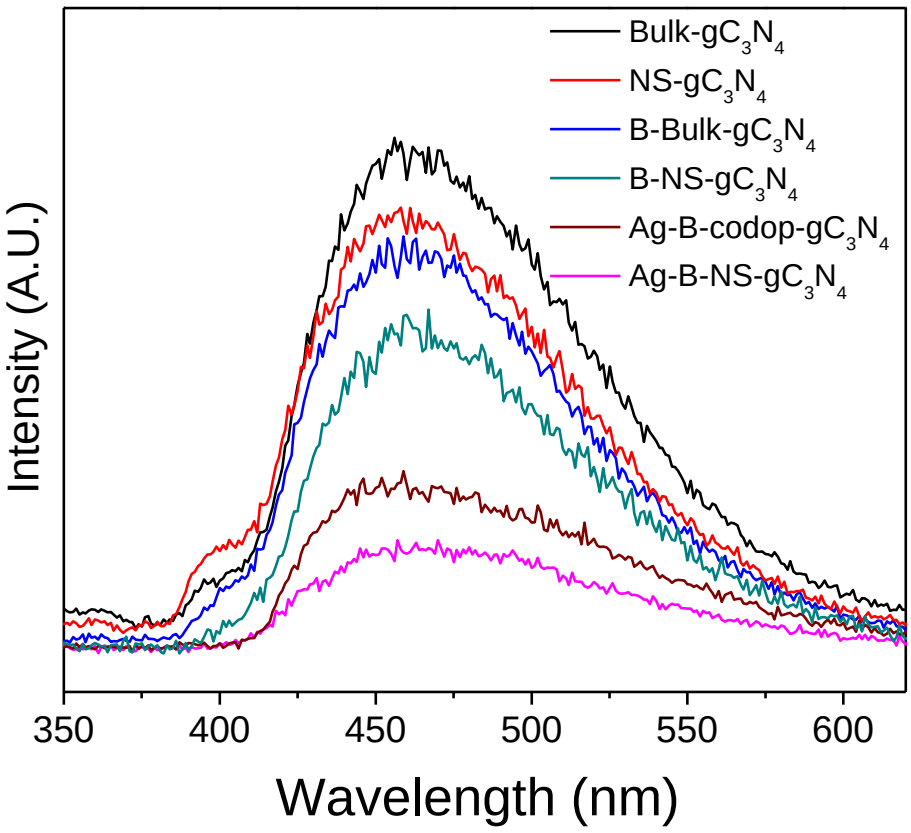

Fig. 5: Photoluminescence emission spectra of bulk-gC_3N_4, NS-gC_3N_4, B-bulk-gC_3N_4, B-NS-gC_3N_4, Ag-B-bulk-gC_3N_4 and Ag-B-NS-gC_3N_4 samples.

.

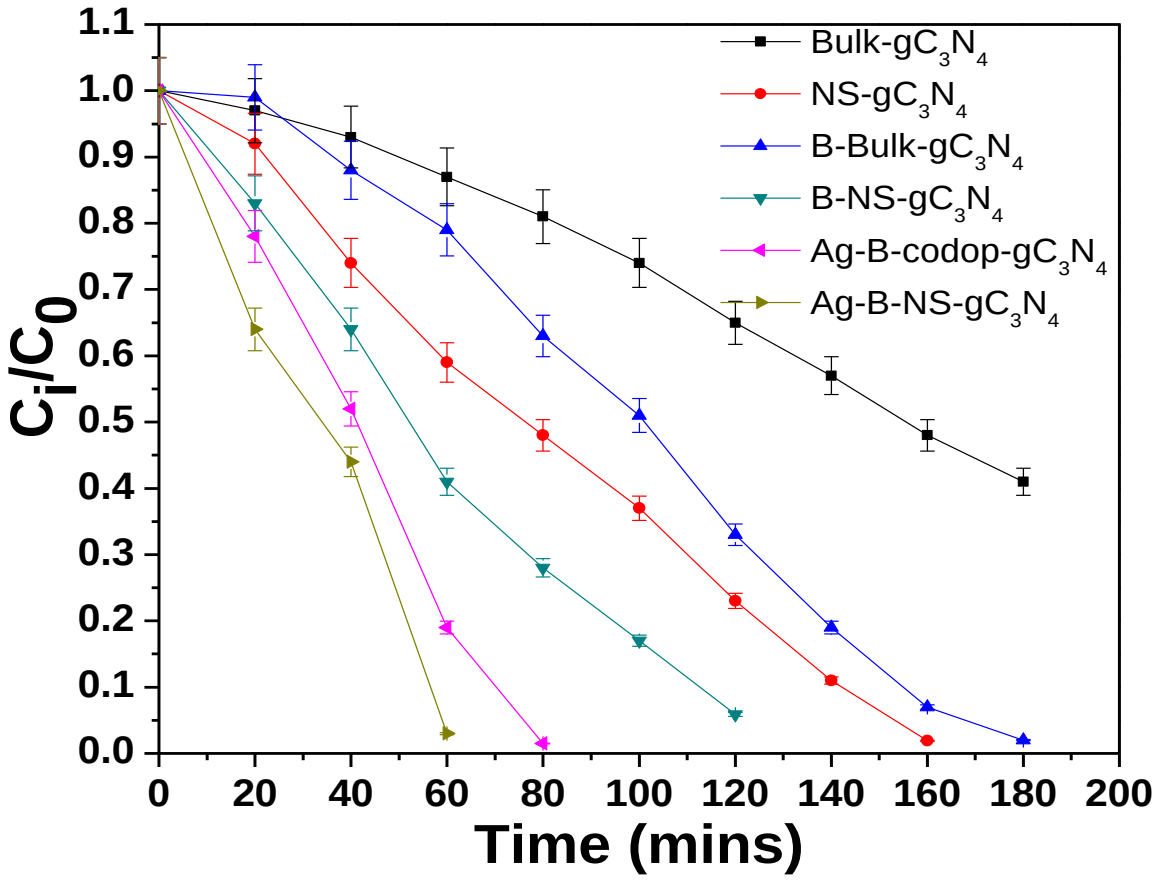

Fig. 6: Comparison of photocatalytic degradation of Rh B under light irradiation in presence of bulk-gC_3N_4, NS-gC_3N_4, B-bulk-gC_3N_4, B-NS-gC_3N_4, Ag-B-bulk-gC_3N_4 and Ag-B-NS-gC_3N_4 samples.

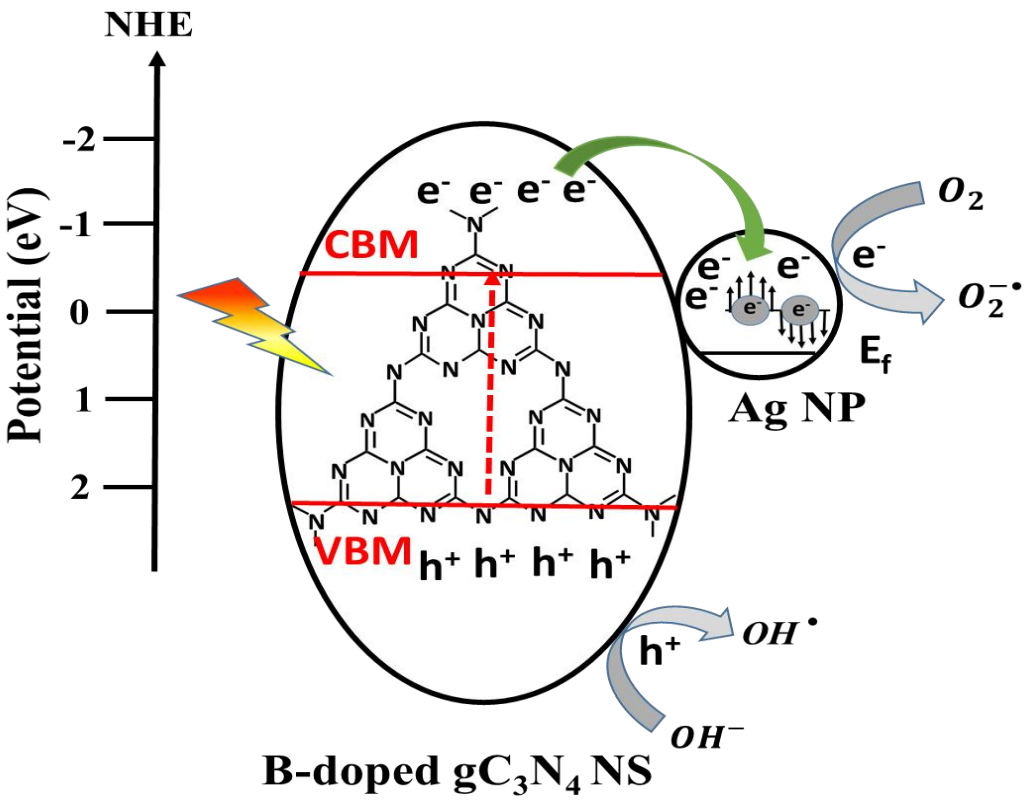

Fig. 7: Mechanism involving charge separation in Ag loaded B-NS-gC_3N_4 during photodegradation of RhB under light illumination.

Table 1: BET surface area of bulk-gC_3N_4, NS-gC_3N_4, B-bulk-gC_3N_4, B-NS-gC_3N_4, Ag-B-bulk-gC_3N_4 and Ag-B-NS-gC_3N_4 samples.

Samples name	**Surface area (sq. m/gm)**
bulk-gC_3N_4	29.07 ± 0.29
NS-gC_3N_4	49.47± 0.74
B-bulk-gC_3N_4	34.18± 0.48
B-NS-gC_3N_4	57.27± 0.91
Ag-B-NS-gC_3N_4	49.64± 0.64
Ag-B-bulk-gC_3N_4	38.91± 0.42